Nanoscale Advances

ROYAL SOCIETY OF CHEMISTRY

PAPER

View Article Online
View Journal | View Issue

Check for updates

Cite this: *Nanoscale Adv.*, 2024, **6**, 5409

Growth mechanism of 2D heterostructures of polypyrrole grown on TiO_2 nanoribbons for high-performance supercapacitors†

Abeer Enaiet Allah *[a,b] and Fatma Mohamed[a,b,c]

Received 8th February 2024
Accepted 14th August 2024

DOI: 10.1039/d4na00121d

rsc.li/nanoscale-advances

The patterning of functional structures is crucial in the field of materials science. Despite the enticing nature of two-dimensional surfaces, the task of directly modeling them with regular structures remains a significant challenge. Here we present a novel method to pattern a two-dimensional polymer in a controlled way assisted by chemical polymerization, which is confirmed through discernible observation. The fabrication process involves *in situ* polymerization to create 2D layers of polypyrrole (PPy) on extended 2D TiO_2 nanoribbons, resulting in oriented arrays known as 2D PPy/TiO_2. These arrays exhibit enhanced electrochemical performance, making them ideal for supercapacitor applications. The skeleton structure of this material is distinctive, characterized by a homogeneous distribution of layers containing various elements. Additionally, it possesses a large contact surface, which effectively reduces the distance for ion transport and electron transfer. The 2D PPy/TiO_2 electrode has a maximum specific capacitance of 280 F g^{-1} at an applied current density of 0.5 A g^{-1}. Moreover, it demonstrates excellent rate capability and cycling stability. Therefore, this approach will open an avenue for improving polymerization-based patterning toward recommended applications.

1 Introduction

The ability to pattern two-dimensional (2D) nanomaterials with unique structural aspects and well-defined architectures is highly attractive to materials science researchers for energy-storage applications.[1–3] Two-dimensional geometries have unique properties including high aspect ratios, electronic conductivity, and large surface area; however, directly patterning them with a regular structure is still a major challenge.[4–6] In the past decade, there has been a gradual shift in research design from materials synthesis to materials engineering and surface modification for practical applications.[7–10] Inspired by the impressive progress of metal oxides, metal oxide-like 2D nanosheets and their composites have been widely investigated.[11–13] Among them, titanium oxide nanosheets are exceptionally rich in versatile properties such as availability, environmental friendliness, low cost, and electronic properties. Therefore, they show great potential in catalysis, electronics, energy storage, and conversion applications.[13] Indeed, 2D titanium oxide nanosheets with high stability, flexibility, and a large specific surface area are exquisite building backbones for constructing architectures.[14–16] The advantage of using 2D TiO_2 nanosheets is that both faces of this material can be utilized for the uniform growth of functional composites such as 2D titanium oxide nanosheets/conducting polymers with unique structures for charge storage.[11] Conducting polymers with intrinsic properties exhibit high electron affinity, good electrical conductivity, and redox behavior, which provide different electronic and electrochemical properties.[17,18] Particularly, polypyrrole (PPy) is considered one of the pioneering conducting polymers in electrochemistry due to its various promising properties such as ease of synthesis, flexibility, high electrical conductivity, stability, and redox behavior, which have been considered benchmarks for electrode materials used in energy storage applications.[7,17,19–21]

Recent research has been devoted to designing 2D nanostructures with rational architectures that combine conducting polymers and metal oxide nanostructures as electrodes, which can remarkably improve the electrochemical performance of electrode materials. Such composites combine the inherent advantages of each building block and also offer remarkable new properties as a result of the synergistic combination of two different materials. Notably, 2D TiO_2 not only provides a large surface area for the growth and immobilization of conducting polymers such as PPy but also enables strong coordination bond formation between the metal centers of TiO_2 and nitrogen atoms in conducting polymers such as polyaniline (PANI) or

---

[a] *Department of Chemistry, Faculty of Science, Beni-Suef University, 62514 Beni-Suef, Egypt. E-mail: abeer.abdelaal@science.bsu.edu.eg*

[b] *Materials Science Lab, Chemistry Department, Faculty of Science, Beni-Suef University, Beni-Suef 62514, Egypt*

[c] *Nanophotonics and Applications Lab, Faculty of Science, Beni-Suef University, Beni-Suef 62514, Egypt*

† Electronic supplementary information (ESI) available. See DOI: https://doi.org/10.1039/d4na00121d

polypyrrole (PPy), which support the controllable growth of 2D conducting polymers onto the 2D TiO_2 nanosheet surfaces. Furthermore, the transition metal centers of TiO_2 and the N atoms of PPy endow the composite with additional pseudocapacitance.[22]

Supercapacitors have received significant attention in memory backup, hybrid electric vehicles, customer electronics, cell phone towers, communication, and transportation systems due to their superior power delivery, long-life durability, and high cycle stability.[23–26]

In the context of active materials of electrodes and charge storage mechanisms, supercapacitors can be classified into two categories. The first one is electrochemical double-layer capacitors (EDLCs), which store charge electrostatically by forming a double layer of electrolyte ions on the active materials. However, their low energy densities constrain their practical application. The other is pseudocapacitors with high capacitance derived from faradaic redox reactions on the surface of active materials. Nevertheless, pseudocapacitors often suffer from weak stability during cycling owing to redox reactions. Increasing the stability and power density and extending the cycling durability have become areas of deep research focus to meet the demands of high-power delivery/uptake electronics.[26,27] Controlling the material pattern and structure is crucial for supercapacitor electrodes to boost their energy and power density by exposing both surfaces of 2D titanium oxide nanosheet/PPy. Additionally, PPy conductivity and uniform particle size are vital factors for improving the specific capacitance and the rate performance of electrodes in supercapacitors.[28]

Herein, an innovative design of heterostructures composed of 2D titanium oxide nanosheets and PPy is presented for the first time. The 2D titanium oxide nanoribbons act as a template skeleton for the growth of polypyrrole by interfacial polymerization. When the newly designed heterostructure is used as an electrode material for supercapacitor applications, it exhibits an attractive specific capacitance of 280 F g^{-1} at 0.5 A g^{-1}, excellent rate capability, and impressive cycling stability.

2 Materials and methods

2.1. Synthesis of pure TiO_2 nanoribbons

Typically, a homogeneous solution of TiO_2 was obtained by dispersing 4 gm of TiO_2 commercial powder in 400 mL of 10 M NaOH for 30 min. Then, hydrothermal treatment was performed at 170 °C for 24 h. After filtration and washing with deionized water, a multilayered TiO_2 nanosheet was obtained. Finally, the nanopowder was dried overnight and annealed at 500 °C for 3 h.

2.2. Synthesis of 2D PPy/titanium oxide nanosheets

2D TiO_2 was dispersed in 20 mL chloroform containing 0.05 M pyrrole by ultrasonic treatment for 1 h. Then, another solution of 0.05 M potassium persulfate in 20 mL hydrochloric acid was sonicated for 1 h and added to the above suspension. Next, the suspension was left for 2 h until a black-brown precipitate was formed at the interface of the immiscible solutions. During the formation of that precipitate, multiple samples were withdrawn every 30 mn for monitoring the growth of PPy on the TiO_2 surface by TEM. After separation and washing, the precipitate was dried for 24 hours at room temperature.

2.3. Characterization of the prepared nanostructures

The morphology of the samples was characterized using a high-resolution transmission electron microscope (HR-TEM, JEOL-2010F). The wide-angle X-ray diffraction (XRD) patterns were acquired on an XRD (Philips X'Pert Pro MRD). Finally, Fourier Transform Infrared Spectroscopy (FTIR) was performed using a Shimadzu-FTIR-340-Jasco spectrometer to show the important functional groups of the samples.

2.4. Electrode preparation

The as-prepared 2D TiO_2 and 2D PPy/TiO_2 samples were ground before preparing the inks. In a typical procedure, 2.0 mg of sample was dispersed in 400 μL of isopropanol/water mixed solvent (with a volume ratio of 1/2) containing 20 μL of 5.0 wt% Nafion solution and sonicated for at least 30 min to form a homogeneous ink. Next, 200 μL of the obtained suspension was added dropwise onto flexible graphite paper (thickness: 1 mm) with an area of 1×1 cm^2 and dried at 60 °C. All electrochemical measurements were carried out on a CHI 660E instrument. In a three-electrode system, the as-prepared working electrodes of 2D TiO_2 and 2D PPy/TiO_2 samples were investigated by cyclic voltammetry (CV) and galvanostatic charge–discharge (GCD) in 1 M H_2SO_4 electrolyte, with a platinum wire as the counter electrode and a saturated calomel electrode (SCE) as the reference electrode, by using cyclic voltammetry (CV) and galvanostatic charge–discharge (GCD). The specific capacitance of the as-made electrodes was calculated from GCD curves. The test of long-term stability for 2D PPy/TiO_2 was conducted by cycling it between 0.0 and 0.8 V *vs.* Ag/AgCl in 1 M H_2SO_4 at a scan rate of 100 mV s^{-1}.

For two electrode system measurements, two identical flexible graphite papers (thickness: 1 mm) with an area of 1×1 cm^2 were used in 1 M H_2SO_4. 200 μL of previously prepared ink with a mass loading of 1 mg was drop-cast on each graphite sheet.

The gravimetric specific capacitance (C_g, F g^{-1}) was calculated using the following:

$$C = \frac{I \times t}{m \times \Delta V} \tag{1}$$

where I is the discharge current (A), t is the discharge time (s), m is the mass of active material (g), and ΔV is the potential change during the discharge process (V).

Energy density and power density can be calculated according to the following equations.

$$E = \frac{1}{2} C_{\text{cell}} V^2 \tag{2}$$

$$P = \frac{E}{\Delta t} \tag{3}$$

3 Results and discussion

X-ray diffraction can be used to determine the crystallinity. PPy is a widely used polymer compound that exhibits conductivity. The structure is characterized by a conjugated long chain. Consequently, a longer molecular chain results in a larger number of electrons and a more orderly arrangement of the molecular chain, thus enhancing the conductivity of electrons. These peaks are commonly found at precise 2θ angles. The XRD pattern of PPy exhibits a high degree of crystallinity, as depicted in Fig. 1. The presence of strong hydrogen bonding and electrostatic interactions between phenolic and amine groups in the polymer chain is indicated by the distinct peaks seen at 6.46°, 23°, and 28.21° in Fig. 1.[29]

The XRD pattern of titanium nanosheets shows the formation of mixed phases from the rutile and anatase phases of TiO_2, as shown in Fig. 1, according to JCPDS numbers 88-1175 and 84-1286. The XRD pattern of 2D titanium oxide nanosheets shows distinct strong diffraction peaks at 11.3°, 27°, 36°, 47°, and 58.7°, which are attributed to rutile TiO_2. In addition, the diffraction peaks at 25° and 48° correspond to the presence of TiO_2 in the anatase phase.[30] In contrast to TiO_2, 2D titanium oxide nanosheet/PPy shows a mixed phase between TiO_2 and PPy, which enhances the crystallinity of the 2D PPy/TiO_2 hybrid. The small hump that appeared in the PPy polymer matrix at 2θ between 17°–19° shifted to a higher value of 21° and became narrow due to the interaction between the TiO_2 and polymer matrix.[31] The peak located at 29° in the hybrid is attributed to the combination of a peak at 29.7° of TiO_2 and a peak at 29° for the polymer, which is probably due to the interaction between the pyrrole units and TiO_2, *i.e.*, the polymerization of pyrrole is followed by the adsorption of pyrrole on TiO_2.[32] In addition, Fourier-transform infrared (FTIR) spectroscopy was commonly employed to examine the chemical bonds of PPy. The FTIR peaks of PPy in Fig. 2 exhibited a feature at 1330 cm^{-1}, corresponding to in-plane C–H bending vibrations. Additionally, a peak at 1193 cm^{-1} was found, indicating C–N–C stretching vibrations. The C–C asymmetrical and symmetrical stretching vibrations were detected at 1560 and 1477 cm^{-1}, respectively. The existence of additional functions, including N–H/O–H, C–O, and C=O, was also verified using the characteristic stretching vibrations at 3370, 1115, and 1633 cm^{-1}, respectively. The band at 850 cm^{-1} corresponds to C–H band oscillation.[33] From the infrared spectrum of chemically synthesized TiO_2, the sharp absorption band around 500 cm^{-1} was attributed to the Ti–O and Ti–O–Ti stretching vibrations of TiO_2.[34] Other bands were observed at 1400 and 1620 cm^{-1}, which are assigned to Ti–O, Ti–OH, and O–H stretching, which were formed through strong hydrogen bonding. Moreover, there is a noticeable broad peak around 3500 cm^{-1}, which is ascribed to the OH function group.[29,33,35,36]

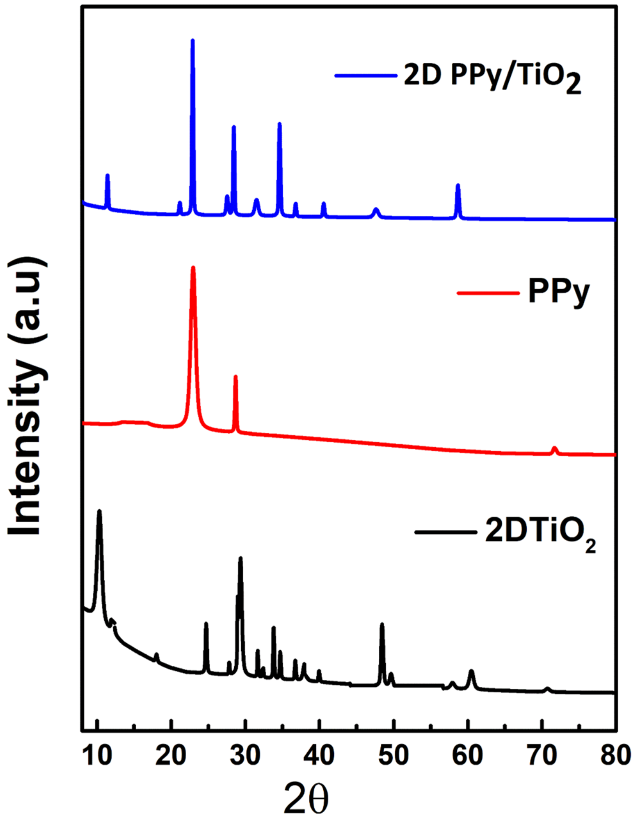

Fig. 1 XRD patterns of 2D TiO_2, PPy and 2D PPy/TiO_2.

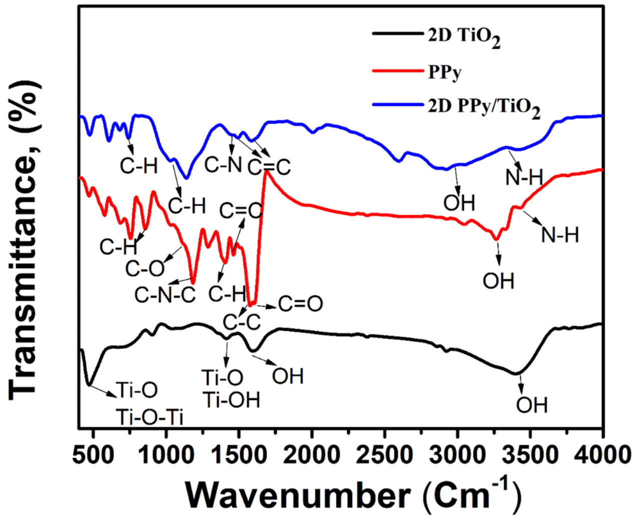

Fig. 2 FTIR of the prepared samples: TiO_2, PPy, and 2D PPy/TiO_2.

The FTIR spectrum of the 2D PPy/TiO_2 is illustrated in Fig. 2, and all the characteristic peaks of PPy can be observed. The N–H stretching vibration peak is observed at 3413 cm^{-1}. The broadening of the peak located at 2500–3600 cm^{-1} demonstrates the presence of OH on the surface of adsorbed water.[37] The chemical interaction between PPy and TiO_2 could be explained by the low intensities of the peaks in the range of 2500–3600 cm^{-1}, with the position shifted to a lower wavenumber.[38]

The peaks at 1590 cm^{-1} and 1495 cm^{-1} correspond to C=C, and the peak at 1460 is ascribed to C–N stretching vibration in the pyrrole ring. The deformation of N–H and the vibration of C–H is indicated by two peaks at 1024 cm^{-1} and 1134 cm^{-1},

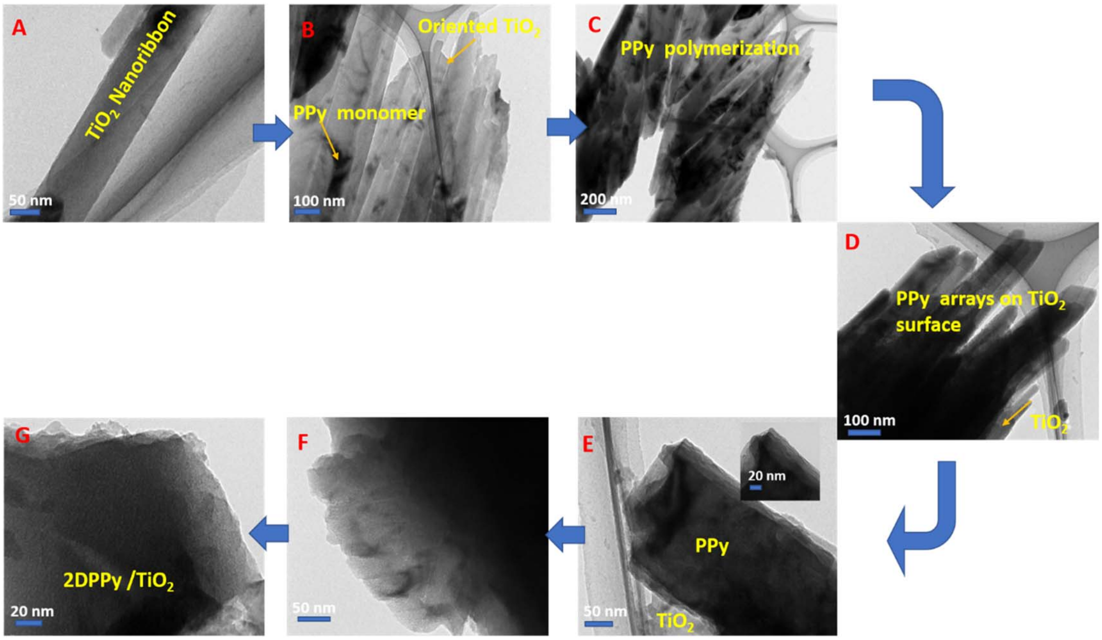

Fig. 3 TEM images of 2D PPy/TiO_2 samples obtained at different reaction intervals as steps for the nucleation and growth mechanisms of PPy nanoribbons: homogeneous nucleation in bulk solution and heterogeneous nucleation on TiO_2 nanosheets: (A) formation of nanoribbons, (B) at 30 min, heterogeneous nucleation of the PPy monomer on the surface of TiO_2 and the orientation of TiO_2 side by side, (C) at 60 min, initiation of PPy polymerization on the surface of TiO_2, (D and E) at 90 min, self-assembly of PPy as horizontal arrays on the surface of conjugated TiO_2, and (F and G) at 120 min transformation of TiO_2 nanoarrays into 2D successive layers around the TiO_2 backbone.

respectively; the peaks that appear below 740 cm^{-1} correspond to the characteristic peaks of TiO_2. The band at 750 cm^{-1} is assigned to C–H band oscillation. The split peak of C–H plane-bending vibration appears at 1024, confirming the strong interaction between the PPy and nanocrystalline 2D TiO_2.[32] Based on the TEM observation, the formation mechanism of the 2D PPy/TiO_2 composite is depicted schematically in Fig. 3. As for bare TiO_2, a 1D nanoribbon is regarded as a typical intrinsic building unit obtained in the initial stage, as previously reported (Fig. 3A).[39] Subsequently, the early stages of the chemical oxidative polymerization of pyrrole on the TiO_2 nanoribbon surface in the presence of APS led to the heterogeneous nucleation of the monomer and the formation of the oriented conjugated structure of TiO_2 side by side (Fig. 3B).[35]

The dispersibility and hydrophilicity of TiO_2 nanoribbons in an aqueous solution would ensure ample active sites, thereby facilitating good adsorption of monomers onto their surface. Obliviously, the strong coordination and interactions between the Ti metal centers of TiO_2 and the N groups of pyrrole monomers can be seen as dark patches anchored on the TiO_2 surface, which act as the nucleus for the initiation of polymerization, as shown in Fig. 3C. The linear chain structure and expanded nature of the PPy chains enable them to stimulate their self-assembly in horizontal arrays on the surface of conjugated TiO_2, and this will significantly enhance the crystalline features in good agreement with the XRD result (Fig. 3D and E). Therefore, the aggregation of PPy nanoparticles on the TiO_2 scaffold is not observed in the composites. Interestingly, at the terminal stage of polymerization, the assembled arrays of PPy/TiO_2 transformed into 2D PPy successive layers around the TiO_2 backbone, as confirmed by TEM direct observation (Fig. 3F, G and S1†).

The TEM description in Fig. 4a revealed the flat consecutive layers of PPy on the TiO_2 surface in a 2D porous structure. Further analysis confirmed the lateral close-packing arrangement of PPy into TiO_2 surfaces in a distinct architecture (Fig. 4b and c). Close examination of the 2D PPy/TiO_2 composite presents a porous structure, which can be seen clearly in the TEM image in Fig. 4d. Such a porous structure will not only confer diffusion pathways for the electrolyte ions but also provide plentiful networks for electron transfer.

The high-angle annular dark-field scanning transmission electron microscope (HAADF-STEM) image reveals a porous matrix with a 2D structure of PPy on the surface of TiO_2 (Fig. 4e and S2†). In addition, the homogeneous growth of PPy on the TiO_2 surface is further recognized by the corresponding elemental mapping (Fig. 4f–i), in which Ti, C, N, and O elements are distributed homogeneously over the TiO_2 surface, which is in agreement with TEM results and EDX results, as shown in Fig. S3.†

Supercapacitors have received specific attention due to their good safety, long life cycle, high stability, and large power density. Generally, materials with high porosity, 2D structures, and unique electrical conductivity are indispensable for achieving high capacitance and rate capability. Owing to its unique structural advantages, high electrical conductivity, abundant pores, and layer-by-layer structure, the heterostructure of 2D PPy/TiO_2 is expected to be a promising electrode

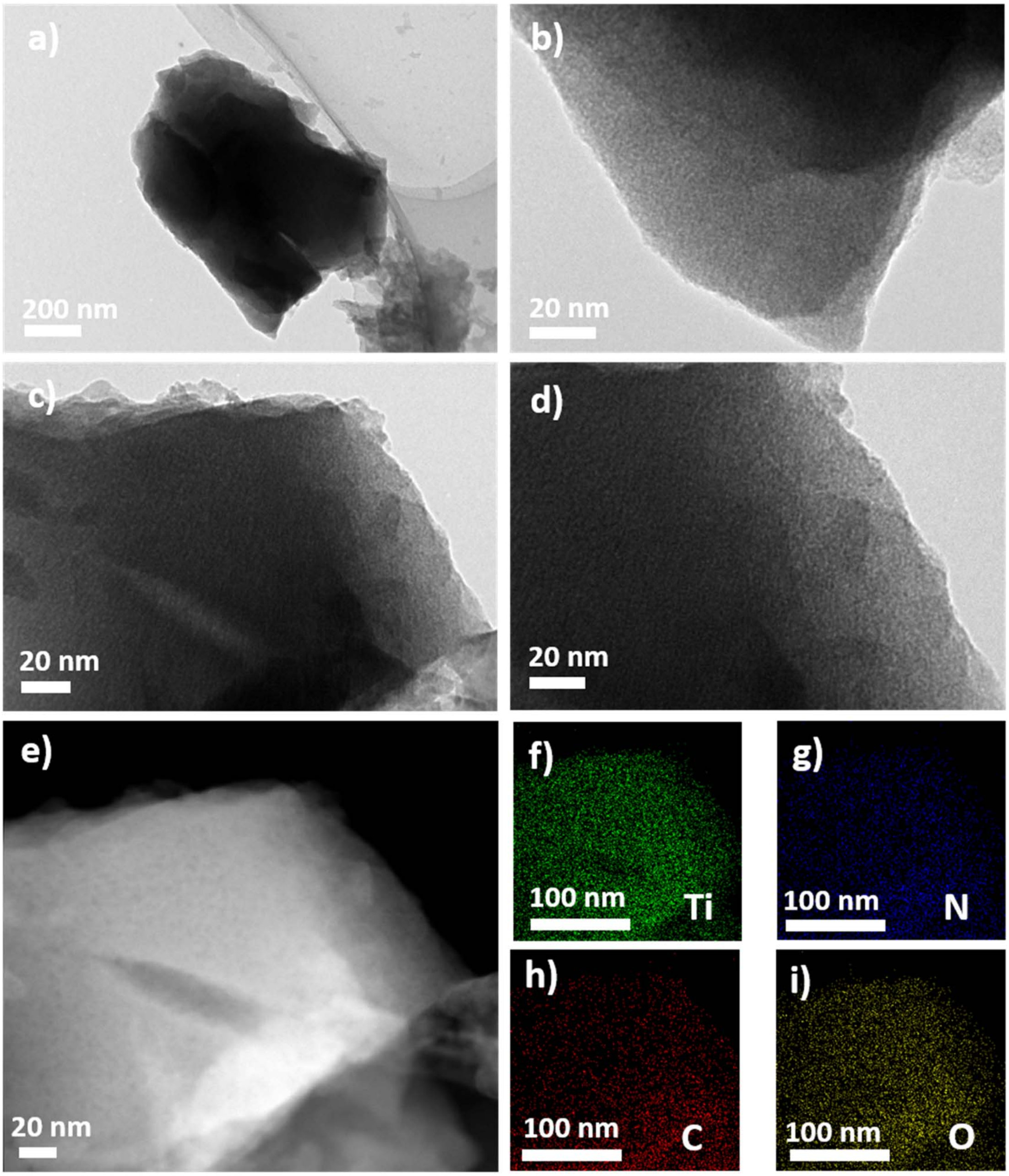

Fig. 4 The structural characterization of 2D PPy/TiO_2: (a–d) TEM image of 2D PPy/TiO_2. (a) Top view of 2D layers of 2D PPy/TiO_2. (b–d) Lateral view of 2D PPy/TiO_2 displaying the close-packing arrangement of PPy into TiO_2 surfaces in porous consecutive layers. (e–i) HAADF-STEM images of 2D PPy/TiO_2, with the corresponding elemental mapping images for titanium, nitrogen, carbon, and oxygen of 2D PPy/TiO_2.

material for practical supercapacitors. To show the superiority of 2D PPy/TiO and to confirm the synergistic effect between TiO_2 and PPy, the electrochemical performances of bare TiO_2 nanosheets and 2D PPy/TiO_2 heterostructures were tested in a three-electrode system using a 1 M H_2SO_4 solution as the electrolyte. Fig. 5a compares the cyclic voltammetry (CV) curves of pure TiO_2 and 2D PPy/TiO_2 electrodes at a scan rate of 5 mV s^{-1}. The CV curves show a rectangular shape, which is typical for double-layer charge storage and is considered an indication of effective polarization at the surface of the electrode. Furthermore, a pair of redox peaks at 0.4/0.5 V indicates a pseudocapacitive behavior, which is due to the partial oxidation of Ti and the pseudo-capacitive behavior of TiO_2.[40,41] Notably, the CV curve of 2D PPy/TiO_2 at 5 mV s^{-1} showed improved capacitive performance and a larger integrated area compared to that of pristine TiO_2 (Fig. 5a), indicating better capacitive properties. Interestingly, at a high scan rate of 300 mV s^{-1}, the CV profiles of both samples display a leaf-like shape with a large area appearing due to the rapid movement of electrolyte ions. This behavior indicates its highly capacitive nature with a significant ion response and high-rate capability. This result could be attributed to the rapid movement of electrolyte ions at a high scan

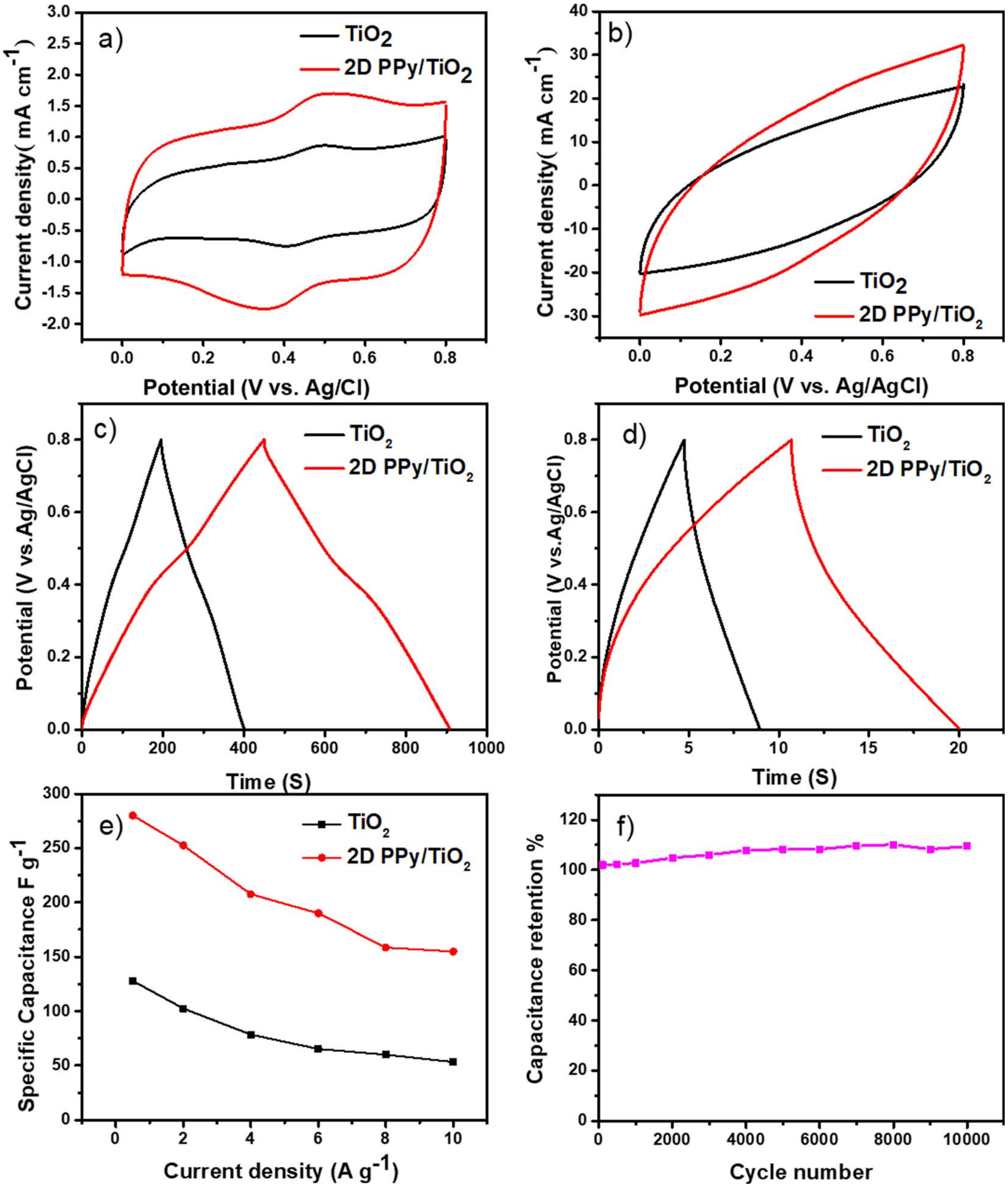

Fig. 5 Electrochemical performances in a three-electrode system. (a) CV curves at a scan rate of 5 mV s^{-1}, (b) CV curves at a scan rate of 300 mV s^{-1}, (c) galvanostatic charge–discharge curves at a current density of 0.5 A g^{-1}, (d) galvanostatic charge–discharge curves at a current density of 10 A g^{-1}, (e) specific capacitances at different current densities for pure TiO_2 and 2D PPy/TiO_2 and (f) cycling performance for 10 000 cycles of 2D PPy/TiO_2 at 100 mV s^{-1}.

rate. This case displays the process of double-layer behavior (Fig. 5b).[42–45] Different scan rates of 5–200 mV s^{-1} in Fig. S4† reveal the good capacitive nature of samples.

The galvanostatic charge/discharge (GCD) curves of the TiO_2 and 2D PPy/TiO_2 electrodes are shown in Fig. 5c, d, and S5a–d†. The GCD curves of 2D PPy/TiO_2 electrodes at different current densities display triangular shapes with symmetric sides, confirming the high capacitive reversibility.[24,46]

The specific capacitances were estimated using the GCD curves (Fig. 5e) of both samples (TiO_2 and 2D PPy/TiO_2). Clearly, at 0.5 A g^{-1}, TiO_2 and 2D PPy/TiO_2 have a specific capacitance of 128 F g^{-1} and 280 F g^{-1}, respectively (Fig. 5c). At a current density of 2 A g^{-1}, 2D PPy/TiO_2 displayed a higher specific capacitance of 252.5 F g^{-1} than TiO_2 with a capacitance of 102.5 F g^{-1} (Fig. S5†). To the best of our knowledge, this value is also higher than those for all the reported TiO_2/polymer composites measured in an aqueous electrolyte using a three-electrode system (Table 1). The capacitances of TiO_2 and 2D PPy/TiO_2 at various current densities from 0.5 to 10 Ag^{-1} are also calculated based on GCD (Fig. 5c, d, and S15a–d†). As expected for 2D PPy/TiO_2, the capacitance value of 2D PPy/TiO_2 surpasses that of pristine TiO_2 at any current density. Moreover, even at

Table 1 Electrochemical performance of 2D PPy/TiO_2 and previously reported titanium/polymer materials in a three-electrode system

Samples	Current density (A g^{-1})	Specific capacitance (F g^{-1})	Electrode stability	Reference
Cu-TCPP@P70	1 A g^{-1}	500	70% capacitance retention after 3000 cycles	19
HybTi@CNFs	1A g^{-1}	280.3	97.5% capacitance retention after 4000 cycles	47
PAN + TiO_2/DBC	100 mV	156	94% capacitance retention after 2000 cycles	48
Ti_3C_2/PPy-2	2 mV s^{-1}	184.36	83% capacitance retention after 4000 cycles	49
PANI-APTEs-TNW	0.2 mA	315	86.8% capacitance retention after 1000 cycles	50
PPy@$Ti_3C_2T_x$/CC	1 A	375	88.7% capacitance retention after 5000 cycles	51
2DPPy/TiO_2	0.5 A g^{-1}	280	110% capacitance retention after 10.000 cycles	This work

a relatively high current density of 10 A g^{-1}, the capacitance value of PPy/TiO_2 is as high as 150 F g^{-1}, displaying a remarkable rate of capacitance retention (54%). Such significant capacitance retention is an indication of easy charge propagation and quick ion transport within the electrode.[22,40,41,52]

To further demonstrate the superiority of 2D PPy/TiO_2, its long-term stability was investigated by CV at 100 mV s^{-1} (Fig. 5d). The capacitance gradually increased until the capacitance retention achieved 110% after 10.000 cycles, possibly due to the activation process of the PPy/TiO_2 electrode by deep successive wetting of the electrolyte through the pores of the material. This result indicates good electrode stability.[53] Further, TEM observation for 2D PPy/TiO_2 after the stability test reveals the maintenance of the morphological structure with small protrusion due to the preparation of the electrode with Nafion and the impregnation of electrolyte through the electrode material matrix, as shown in Fig. S6.†

To further demonstrate the facilitated ion-diffusion kinetics within 2D PPy/TiO_2, electrochemical impedance spectroscopy (EIS) characteristic measurements were carried out for TiO_2 and 2D PPy/TiO_2. Typical Nyquist plots obtained in the frequency range from 100 kHz to 0.01 Hz are shown in Fig. 6. They consist of a small arc in the high-frequency region and a line in the medium to low-frequency region. The semicircle in the high-frequency range is related to the resistance of interfacial charge transfer between the electrode and electrolyte R_{ct} due to the intrinsic resistance of the active material and the ionic resistance of the electrolyte.[54] The metallic nature of TiO_2 endows it with low R_{ct}, and a further decrease in the R_{ct} of the 2D PPy/TiO_2 heterostructure confirms the good interfacial contact between the TiO_2 substrates and the 2D PPy layers, good charge transfer properties, and improved electrochemical activity.[7] Notably, the 2D PPy/TiO_2 electrode shows a shorter and steeper gradient than the pure TiO_2 electrode in the low-frequency region, implying faster ion diffusion capability.[55]

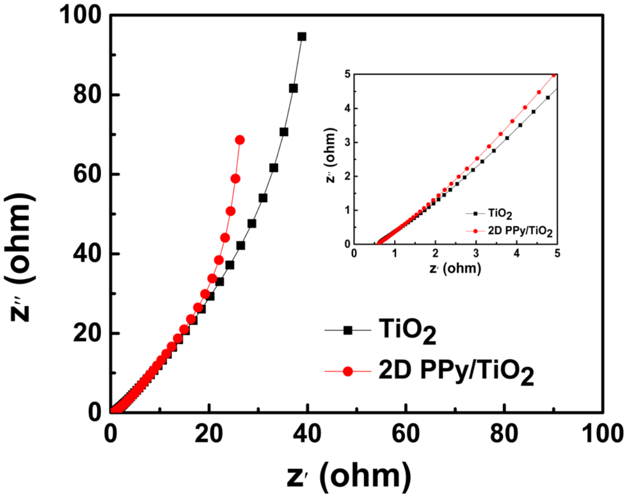

Fig. 6 Nyquist plots of pure TiO_2 and 2D PPy/TiO_2 (inset: close-up view of the high-frequency regime).

To further investigate the performance of pure TiO_2 and 2D PPy/TiO_2 as electrode materials for supercapacitors, electrochemical measurements were also conducted using a symmetric cell. Fig. 7a and b show the CV curves of the symmetrical supercapacitor at 5 mV s^{-1} in the potential window of 0–0.8 V. The CV curves of both samples maintain an optimal rectangular shape with a redox peak, the same as shown in the three-electrode system measurements with improved behavior for 2D PPy/TiO_2 compared to TiO_2. At different high scan rates as shown in Fig. 7c and d, the CV profiles of both samples display a leaf-like shape due to the rapid movement of electrolyte ions at high scan rates.

The charge discharge curves of pure TiO_2 and 2D PPy/TiO_2 in Fig. 8 exhibited a symmetrical triangular shape, suggesting good electrochemical capacitive behavior and excellent reversibility of the charge/discharge cycle due to the contribution of the pseudocapacitive and EDLC behavior of the electrode materials owing to the presence of TiO_2 and 2D PPy. Clearly, increasing current density causes a decrease in charging/discharging time and capacitance. This behavior is attributed to the requirement of less time for the attainment of the same potential difference across the two electrodes at a higher current density value, indicating superior rate capability.[55,56] Obviously, 2D PPy/TiO_2 achieved a higher specific capacitance of 182 F g^{-1} as compared to 85 F g^{-1} for bare TiO_2 at 0.5 A g^{-1}. The increment of specific capacitance from 85 F g^{-1} in TiO_2 to 182 F g^{-1} in 2D PPy/TiO_2, which is nearly two times, could be ascribed to the synergistic combination of electric double-layer capacitance and pseudocapacitance.

As previously discussed for 2D PPy/TiO_2, the huge 2D exposed surface of a layered structure in an open layer-by-layer structure, with redox-active sites, contributed to pseudocapacitance, so the

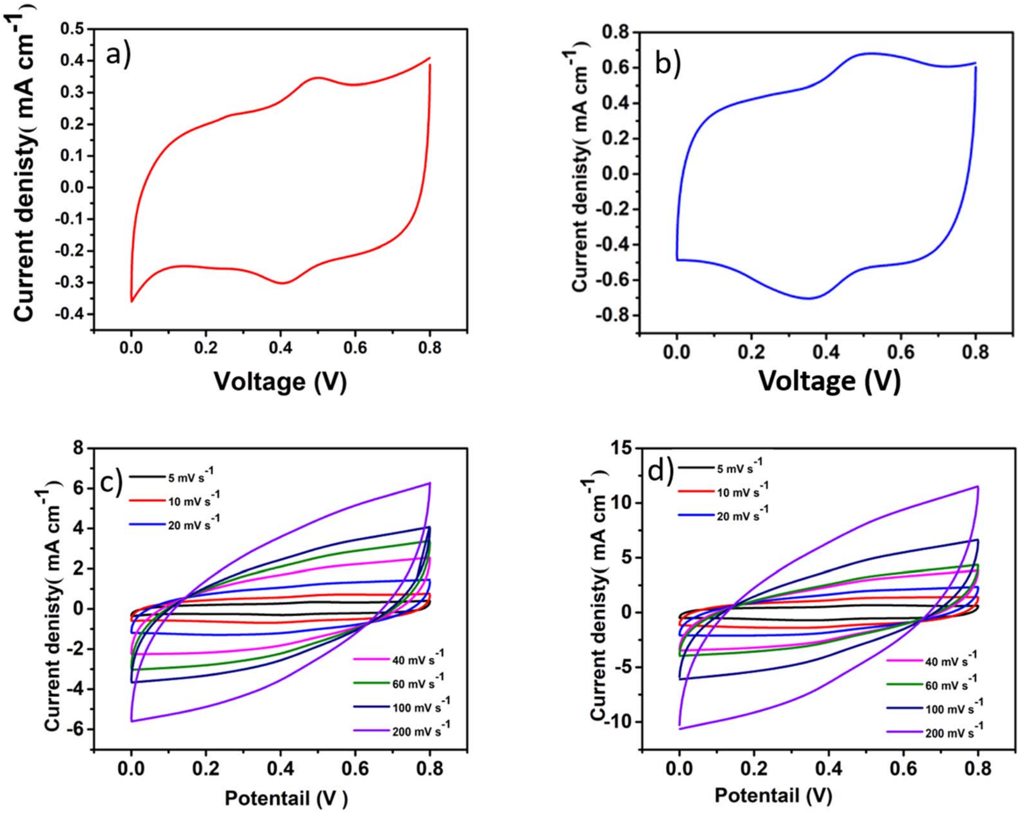

Fig. 7 CV curves of (a) 2D TiO_2 and (b) 2D PPy/TiO_2 at 5 mV^{-1}, CV curves of (c) TiO_2 and (d) 2D PPy/TiO_2 in a two-electrode system at different scan rates.

charge/discharge kinetics is qualitatively evaluated according to the following equations:

$$i = av^b \tag{4}$$

$$\log(i) = \log(a) + b\log(v) \tag{5}$$

where i and v are the current density and scan rate, while a and b are constants, respectively. Generally, the charge storage process depends on the value of the exponential index b. $b = 1$ or close to 1 indicates that electric double-layer capacitance, which controls electrochemical behavior, is a surface-confined process with quick reaction kinetics. When b is close to 0.5, pseudocapacitance with slow reaction kinetics is the predominant electrochemical behavior, indicating a diffusion-controlled reaction mechanism. Fig. 9a presents the relationship between $\log(i)$ and $\log(v)$. The calculated b values for TiO_2 and 2D PPy/TiO_2 ranged from 0.61 to 0.63 in the charging process and from 0.56 to 0.58 in the discharging process, which confirms that the electrochemical behavior is dominated by pseudocapacitance[56–58]

The percentage contributions of both electric double-layer capacitance (C_{EDL}) and pseudocapacitance (C_{PC}) to the total specific capacitance were calculated using the Trasatti method. Fig. 9b displays the plotting of the inverse of specific capacitance ($1/C$) against the square root of the scan rate. According to eqn (6), the Y-intercept of the linearly fitted line in the low scan rate region (Fig. S7†) provided the inverse of the total specific capacitance (C_T) of the electrode materials. Moreover, Fig. 9C plots the specific capacitance (C) *versus* the inverse square root of the scan rate in order to calculate C_{EDL}. The value of the y-intercept obtained by plotting the fitted line in a high scan rate region (Fig. S8†) represents C_{EDL} according to the following equations.

$$\frac{1}{C} = k_1\sqrt{v} + \frac{1}{C_T} \tag{6}$$

$$C = k_2\frac{1}{\sqrt{v}} + C_{EDL} \tag{7}$$

The contribution of pseudocapacitance (C_{PC}) was calculated by subtracting C_{EDL} from $C_{T,}$ where k_1 and k_2 are arbitrary constants. The percentage contributions of C_{EDL} and C_{PC} for TiO_2 and 2D PPy/TiO_2 are shown in Fig. 9d. Clearly, TiO_2 has 74% C_{PC} and 26% C_{EDL}, while 2D PPy/TiO_2 has 97.5% C_{PC} and 2.5% C_{EDL}. Furthermore, after the growth of 2D PPy on the surface of TiO_2, the C_{PC} contribution increases to 97.5% due to improved titanium dioxide's electrochemical activity with the addition of highly conductive PPy that accelerates and improves the electron transfer between the conductive state and semiconductive state and facilitates the redox transition of TiO_2. For this reason, the synergy between 2D PPy and TiO_2 nanoparticles increases specific capacitance.[59]

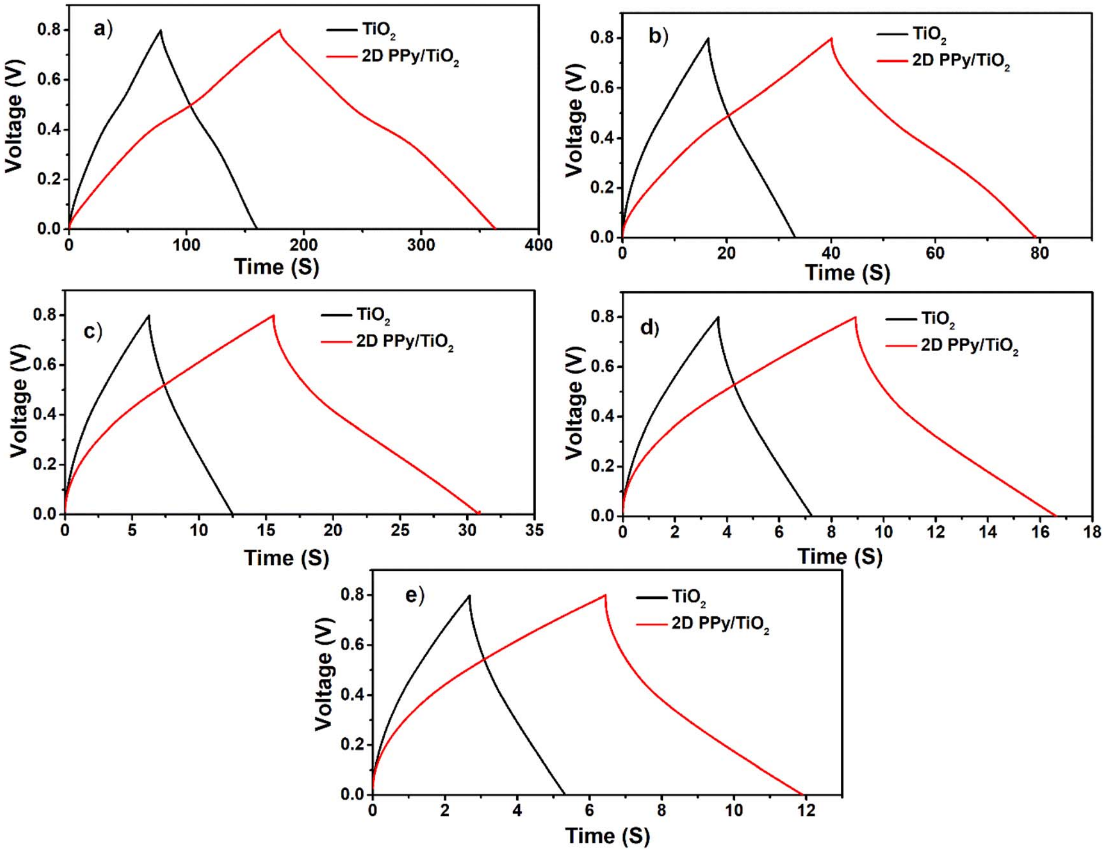

Fig. 8 Galvanostatic charge–discharge curves at a different current densities, (a) 0.5, (b) 2, (c) 4, (d) 8, and (e) 10 A g^{-1}, for pure TiO$_2$ and 2D PPy/TiO$_2$.

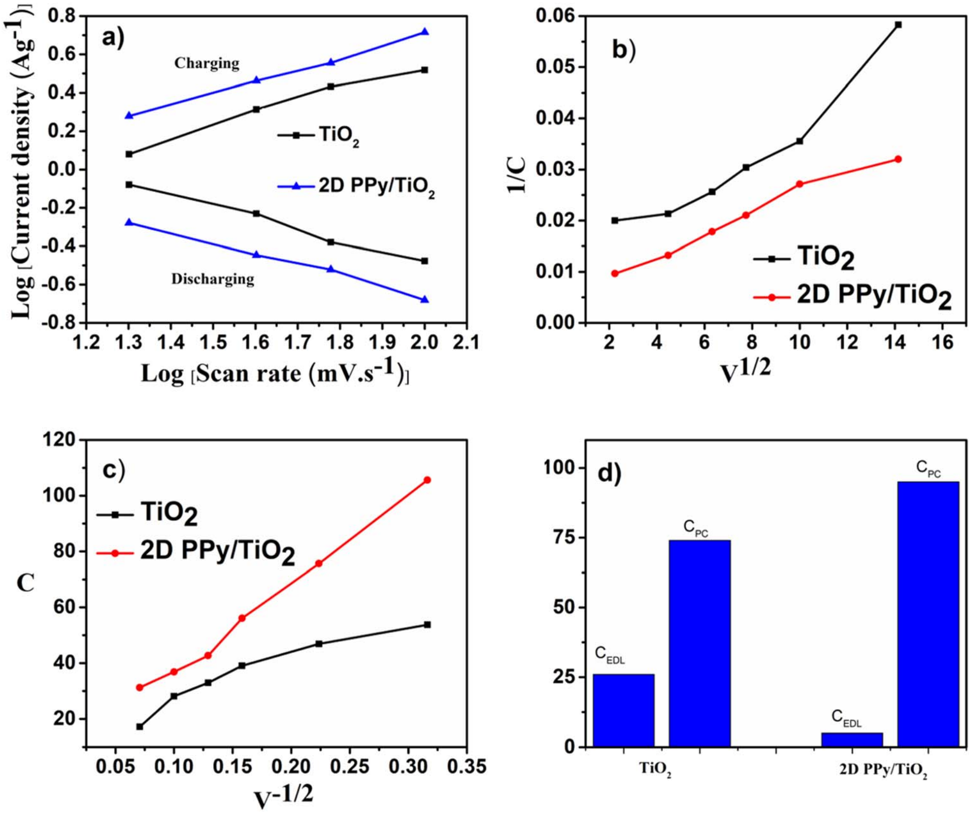

Fig. 9 (a) Linear plot of log *i* *vs.* log *ν* in both charge and discharge processes, (b) plot of 1/*C* *versus* $\sqrt{v}$, (c) plot of c *versus* $1/\sqrt{v}$, and (d) contribution of electric double-layer capacitance and pseudocapacitance for TiO$_2$ and 2D PPy/TiO$_2$.

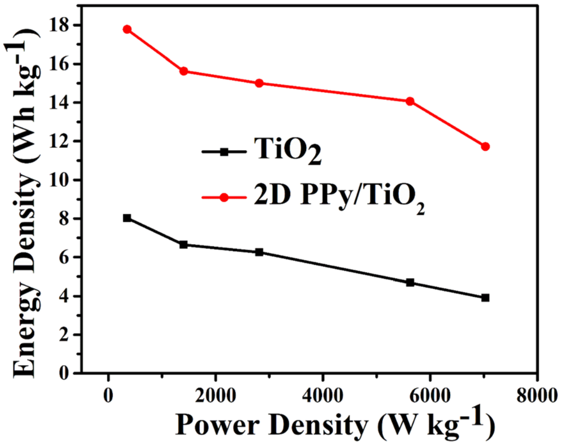

Fig. 10 Ragone plot of TiO_2 and 2D PPy/TiO_2.

To assess the activity of the prepared electrodes in the practical application of supercapacitor devices, the power density (P_s) and energy density (E_s) of electrode materials were calculated and compared as shown in the Ragone plots of TiO_2 and 2D PPy/TiO_2 in Fig. 10. The plot shows that 2D PPy/TiO_2 achieved a higher energy density as compared to bare TiO_2. 2D PPy/TiO_2 displays an energy density of 18.5 Wh kg^{-1} and a power density of 351.5 W kg^{-1} at a current density of 0.5 A g^{-1}, which is 2.3 times higher than that of TiO_2 (13.125 Wh kg^{-1}) at the same current density. These results reflect the synergistic effect of the combination of 2D PPy sheets on the metallic surface of TiO_2. Furthermore, it is outstanding in comparison with previous literature.[56]

4 Conclusion

Two-dimensional polypyrrole PPy on TiO_2 nanoribbons was fabricated, forming an oriented 2D layer. The structural characterization of 2D PPy/TiO_2 was performed by TEM. The nucleation and growth mechanisms of PPy nanosheets involved homogeneous nucleation in bulk solution and heterogeneous nucleation on TiO_2 nanosheets. 2D PPy/TiO_2 displays superior electrochemical properties for supercapacitor applications. The path for electron transfer and ion transport is shortened by a special skeleton structure with a consistent distribution of layers with various constituents. The 2D PPy/TiO_2 electrode has a maximum specific capacitance of 280 F g^{-1} at 0.5 A g^{-1} with good rate capability and cycling stability. Therefore, this strategy will be recommended for enhancing polymerization-based patterning toward supercapacitor applications.

Data availability

All data generated or analyzed during this study are included in this published article (and its ESI† file)

Conflicts of interest

There are no conflicts to declare.

References

1 X. Feng, *Nat. Commun.*, 2015, **6**, 1–9.
2 A. Gopalakrishnan and S. Badhulika, *Fundam. Supercapacitor Appl. 2D Mater.*, 2021, pp. 253–310.
3 X. Xu, T. Liang, D. Kong, B. Wang and L. Zhi, *Mater. Today Nano*, 2021, **14**, 100111.
4 Z. Zhang, J. Du, J. Li, X. Huang, T. Kang, C. Zhang, S. Wang, O. O. Ajao, W. J. Wang and P. Liu, *Prog. Polym. Sci.*, 2021, **114**, 101360.
5 Q. Zhu, J. Li, P. Simon and B. Xu, *Energy Storage Mater.*, 2021, **35**, 630–660.
6 S. Wang, Z. Wang, Y. Huang, Y. Hu, L. Yuan, S. Guo, L. Zheng, M. Chen, C. Yang, Y. Zheng, J. Qi, L. Yu, H. Li, W. Wang, D. Ji, X. Chen, J. Li, L. Li and W. Hu, *ACS Appl. Mater. Interfaces*, 2021, **13**, 17852–17860.
7 H. Tang, J. Wang, H. Yin, H. Zhao, D. Wang and Z. Tang, *Adv. Mater.*, 2014, 1–7.
8 Y. Chen, Z. Fan, Z. Zhang, W. Niu, C. Li, N. Yang, B. Chen and H. Zhang, *Chem. Rev.*, 2018, **118**, 6409–6455.
9 L. Zhang, J. Dong and F. Ding, *Chem. Rev.*, 2021, **121**, 6321–6372.
10 Y. Zhu, L. Peng, Z. Fang, C. Yan, X. Zhang, G. Yu, Y. Zhu, L. Peng, Z. Fang, C. Yan, X. Zhang and G. Yu, *Adv. Mater.*, 2018, **30**, 1706347.
11 M. Kandasamy, S. Sahoo, S. K. Nayak, B. Chakraborty and C. S. Rout, *J. Mater. Chem. A*, 2021, **9**, 17643–17700.
12 H. Xie, Z. Li, L. Cheng, A. A. Haidry, J. Tao, Y. Xu, K. Xu and J. Z. Ou, *iScience*, 2022, **25**, 103598.
13 P. Kumbhakar, C. Chowde Gowda, P. L. Mahapatra, M. Mukherjee, K. D. Malviya, M. Chaker, A. Chandra, B. Lahiri, P. M. Ajayan, D. Jariwala, A. Singh and C. S. Tiwary, *Mater. Today*, 2021, **45**, 142–168.
14 S. B. Patil, H. J. Kim, H. K. Lim, S. M. Oh, J. Kim, J. Shin, H. Kim, J. W. Choi and S. J. Hwang, *ACS Energy Lett.*, 2018, **3**, 412–419.
15 P. Pazhamalai, K. Krishnamoorthy, V. K. Mariappan and S. J. Kim, *J. Colloid Interface Sci.*, 2019, **536**, 62–70.
16 Y. Ma, X. Xie, W. Yang, Z. Yu, X. Sun, Y. Zhang, X. Yang, H. Kimura, C. Hou, Z. Guo and W. Du, *Adv. Compos. Hybrid Mater.*, 2021, **4**, 906–924.
17 S. Sardana, A. Gupta, K. Singh, A. S. Maan and A. Ohlan, *J. Energy Storage*, 2022, **45**, 103510.
18 H. Luo, Y. V. Kaneti, Y. Ai, Y. Wu, F. Wei, J. Fu, J. Cheng, C. Jing, B. Yuliarto, M. Eguchi, J. Na, Y. Yamauchi and S. Liu, *Adv. Mater.*, 2021, **33**, 2007318.
19 H. Yao, F. Zhang, G. Zhang, H. Luo, L. Liu, M. Shen and Y. Yang, *Chem. Eng. J.*, 2018, **334**, 2547–2557.
20 H. Mao, C. Ji, M. Liu, Y. Sun, D. Liu, S. Wu, Y. Zhang and X.-M. Song, *RSC Adv.*, 2016, **6**, 111632–111639.
21 N. S. Shaikh, S. B. Ubale, V. J. Mane, J. S. Shaikh, V. C. Lokhande, S. Praserthdam, C. D. Lokhande and P. Kanjanaboos, *J. Alloys Compd.*, 2022, **893**, 161998.
22 Y. Li, X. Zhao, P. Yu and Q. Zhang, *Langmuir*, 2013, **29**, 493–500.
23 Y. Ma, X. Xie, W. Yang, Z. Yu, X. Sun, Y. Zhang, X. Yang, H. Kimura, C. Hou, Z. Guo and W. Du, *Adv. Compos. Hybrid Mater.*, 2021, **4**, 906–924.

24 J. Cheng, S. Chen, D. Chen, L. Dong, J. Wang, T. Zhang, T. Jiao, B. Liu, H. Wang, J. J. Kai, D. Zhang, G. Zheng, L. Zhi, F. Kang and W. Zhang, *J. Mater. Chem. A*, 2018, **6**, 20254–20266.
25 M. Guan, Q. Wang, X. Zhang, J. Bao, X. Gong and Y. Liu, *Front. Chem.*, 2020, **8**, 1–14.
26 D. Nandi, V. B. Mohan, A. K. Bhowmick and D. Bhattacharyya, *J. Mater. Sci.*, 2020, **55**, 6375–6400.
27 L. Zhang and X. S. Zhao, *Chem. Soc. Rev.*, 2009, **38**, 2520–2531.
28 N. Parveen, M. O. Ansari, T. H. Han and M. H. Cho, *J. Solid State Electrochem.*, 2017, 57–68.
29 A. Abdelfatah, O. F. Abdel-Gawad, A. M. Elzanaty, A. M. Rabie and F. Mohamed, *J. Mol. Liq.*, 2022, **345**, 117034.
30 M. Balamurugan, M. Silambarasan, S. Saravanan and T. Soga, *Phys. B Condens. Matter*, 2022, **638**, 413843.
31 L. H. Gaabour, *AIP Adv.*, 2021, **11**, 105120.
32 X. Ding, H. Shao, H. Wang, W. Yang, J. Fang, D. Zhang and T. Lin, *Nano Energy*, 2021, **89**, 106367.
33 T. Karazehir, *Int. J. Hydrogen Energy*, 2023, **48**, 10493–10506.
34 B. Santara, P. K. Giri, K. Imakita and M. Fujii, *Nanoscale*, 2013, **5**, 5476–5488.
35 A. León, P. Reuquen, C. Garín, R. Segura, P. Vargas, P. Zapata and P. A. Orihuela, *Appl. Sci.*, 2017, **7**, 49.
36 J. Mei, G. Hou, H. Zhang, Q. Chen, H. Cao, Y. Tang, J. Zhang and G. Zheng, *Appl. Surf. Sci.*, 2023, **623**, 156930.
37 M. A. Farea, G. B. Bhanuse, H. Y. Mohammed, M. O. Farea, M. Sallam, S. M. Shirsat, M. L. Tsai and M. D. Shirsat, *J. Alloys Compd.*, 2022, **917**, 165397.
38 M. M. El-Desoky, I. Morad, M. H. Wasfy and A. F. Mansour, *J. Mater. Sci. Mater. Electron.*, 2020, **31**, 17574–17584.
39 A. M. Ahmed, F. Mohamed, A. M. Ashraf, M. Shaban, A. Aslam Parwaz Khan and A. M. Asiri, *Chemosphere*, 2020, **238**, 124554.
40 S. Sundriyal, V. Shrivastav, M. Sharma, S. Mishra and A. Deep, *J. Alloys Compd.*, 2019, **790**, 377–387.
41 Q. Wang, M. Li and Z. Wang, *RSC Adv.*, 2019, **9**, 7811–7817.
42 A. S. F. M. Asnawi, S. B. Aziz, S. R. Saeed, Y. M. Yusof, R. T. Abdulwahid, S. Al-Zangana, W. O. Karim and M. F. Z. Kadir, *Membranes*, 2020, **10**, 1–20.
43 G. P. Pandey, Y. Kumar and S. A. Hashmi, *Solid State Ionics*, 2011, **190**, 93–98.
44 M. H. Hamsan, S. B. Aziz, M. M. Nofal, M. A. Brza, R. T. Abdulwahid, J. M. Hadi, W. O. Karim and M. F. Z. Kadir, *J. Mater. Res. Technol.*, 2020, **9**, 10635–10646.
45 M. Yu, Y. Zeng, C. Zhang, X. Lu, C. Zeng, C. Yao, Y. Yang and Y. Tong, *Nanoscale*, 2013, **4**, 10806–10810.
46 Q. Fu, J. Wen, N. Zhang, L. Wu, M. Zhang, S. Lin, H. Gao and X. Zhang, *RSC Adv.*, 2017, **7**, 11998–12005.
47 S. Aslan, D. Bal Altuntaş, Ç. Koçak and H. Kara Subaşat, *Electroanalysis*, 2021, **33**, 120–128.
48 K. Tang, Y. Li, H. Cao, C. Su, Z. Zhang and Y. Zhang, *Electrochim. Acta*, 2016, **190**, 678–688.
49 W. Wu, D. Wei, J. Zhu, D. Niu, F. Wang, L. Wang, L. Yang, P. Yang and C. Wang, *Ceram. Int.*, 2019, **45**, 7328–7337.
50 P. Zhang, L. Cao, X. Wang, J. Cui, Z. Lin, S. Ngai, F. Vogel, H. Wang, W. Li, S. Li and Q. Wang, *Ceram. Int.*, 2022, **48**, 1731–1739.
51 X. Chen, F. Su, Q. Zhou and J. Sun, *Surface. Interfac.*, 2021, **26**, 101393.
52 Q. Fan, R. Zhao, M. Yi, P. Qi, C. Chai, H. Ying and J. Hao, *Chem. Eng. J.*, 2022, **428**, 131107.
53 A. Enaiet Allah, H. Tan, X. Xu, A. A. Farghali, M. H. Khedr, A. A. Alshehri, Y. Bando, N. A. Kumar and Y. Yamauchi, *Nanoscale*, 2018, **10**, 12398–12406.
54 A. E. Allah, Y. Yamauchi, J. Wang, Y. Bando, H. Tan, A. A. Farghali, M. H. Khedr, A. Alshehri, Y. G. Alghamdi, D. Martin, M. A. Wahab, M. S. A. Hossain and A. K. Nanjundan, *Chemelectrochem*, 2019, 1–8.
55 A. E. Allah, J. Wang, Y. V. Kaneti, T. Li, A. A. Farghali, M. H. Khedr, A. K. Nanjundan, B. Ding, H. Dou, X. Zhang, B. Yoshio and Y. Yamauchi, *Nano Energy*, 2019, **65**, 103991.
56 S. Ansari, R. B. Choudhary and A. Gupta, *J. Energy Storage*, 2023, **59**, 106446.
57 A. Enaiet Allah, F. Mohamed, M. A. Ghanem and A. M. Ahmed, *RSC Adv.*, 2024, **14**, 13628–13639.
58 Y. J. Cao, C. Y. Lu, Z. W. Zhang, Z. Wang, Y. H. Kang, T. T. Yang, G. H. Liu, X. Y. Wei and H. C. Bai, *ACS Omega*, 2022, **7**, 23342–23352.
59 E. Azizi, J. Arjomandi, H. Shi and M. Ali, *J. Energy Storage*, 2024, **75**, 109665.